Energy Advances

ROYAL SOCIETY OF CHEMISTRY

PAPER

View Article Online
View Journal | View Issue

Cite this: *Energy Adv.*, 2026, 5, 419

Exploring performance limits toward 20.79% efficiency in 2D-layered Ruddlesden–Popper perovskite solar cells

Mustafa Kareem, *[ab] Ethar Yahya Salih,[c] Sampangi Rama Reddy B. R,[d] Praveen Priyaranjan Nayak,[e] Sridharan Sundharam[f] and Sanjeev Kumar[g]

Received 12th December 2025,
Accepted 3rd March 2026

DOI: 10.1039/d5ya00364d

rsc.li/energy-advances

Two-dimensional Ruddlesden–Popper (2DRP) halide perovskites have attracted considerable interest in photovoltaics due to their optoelectronic properties and superior environmental stability. Herein, a 2-(methylthio)ethylamine ($MTEA^+$) bulky spacer was introduced as the organic interlayer with sulfur–sulfur bonding, which interacted electrostatically with the inorganic framework to induce the oriented $(MTEA)_2(MA)_4Pb_5I_{16}$ 2DRP perovskite and lattice stabilization. We demonstrated, through numerical simulations, that the performance of 2DRP-based perovskite solar cells (PSCs) could be improved by adapting the perovskite film thickness, trap-state density, parasitic resistances, and temperature. Optical analyses revealed that the 2DRP perovskite dominated light-harvesting in the visible spectrum, while charge transport materials remained largely transparent. PSCs with 2DRP (n = 5) showed a maximum power conversion efficiency (PCE) of 20.79% with an outstanding open circuit voltage (V_{OC}) of 1.49 V under standard AM1.5G illumination. Moreover, the proposed simulation predicted potentially improved thermal stability for the optimized device, theoretically retaining 95% of its initial performance. A simulated PCE of 20.79% represented a theoretical upper limit achievable only under optimized charge dynamic conditions.

1. Introduction

Continuous expansion of the worldwide population and urbanization has led to a rapid rise in energy consumption, leading to a demand for sustainable and economical energy sources.[1] Solar cells are emerging as key solutions to the worldwide energy crisis and climate change.[2,3]

Metal-halide perovskites have not only transformed photovoltaics but also emerged as a multifunctional material for a wide range of optoelectronics, including light-emitting diodes, photodetectors, and lasers, due to their high absorption coefficient, long charge-carrier diffusion length, tunable bandgap, facile solution processability, and defect tolerance.[4] Perovskite solar cells (PSCs) have an important role in photovoltaic technologies because of their low cost, superior optoelectronic characteristics, and steadily increasing power conversion efficiency (PCE).[5] The PCE of three-dimensional (3D) halide PSCs has improved from 3.8% to 27% in recent years, which is comparable with that of silicon photovoltaics.[6] Nevertheless, the instability of 3D halide perovskites is a major hurdle that restricts the commercial progress of perovskite photovoltaics.[7] Conversely, 2D-layered perovskites with atomically fine quantum well frameworks show higher atmospheric stability, in addition to the quantum confinement effect, tunable composition and structure homogeneity and have resulted in beneficial uses in optoelectronics.[8]

2D Ruddlesden–Popper (2DRP) perovskites have garnered significant interest for utilization in PSCs thanks to their enhanced moisture tolerance, improved thermal stability, low self-doping, and suppressed ion migration compared with their conventional 3D counterparts.[9] 2DRP perovskites can be identified by the fundamental chemical formula $A_2B_{n-1}M_nY_{3n+1}$, where Y stands for a halide, M for a divalent metal, and A and B for monovalent cations. 2D perovskites are composed of one or more inorganic layers encased in bulky organic spacers. Strong hydrogen and Coulombic bonds tightly bind spacer ions, greatly enhancing structural stability.[10] However, due to their high exciton binding energies and wide bandgap energies,

[a] College of Remote Sensing and Geophysics, Al-Karkh University of Science, Haifa St., Baghdad 10011, Iraq. E-mail: dr.mustafa@kus.edu.iq
[b] College of Science, University of Warith Al-Anbiyaa, 56001 Karbala, Iraq
[c] College of Energy and Environmental Sciences, Al-Karkh University of Science, Baghdad 10081, Iraq
[d] Department of Physics & Electronics, School of Sciences, JAIN (Deemed to be University), Bengaluru, Karnataka, India
[e] Department of Electronics & Communication Engineering, Siksha 'O' Anusandhan (Deemed to be University), Bhubaneswar, Odisha, 751030, India
[f] Department of Physics, Sathyabama Institute of Science and Technology, Chennai, Tamil Nadu, India
[g] Department of Physics, University Institute of Sciences, Chandigarh University, Mohali, Punjab, India

2DRP perovskites have shown lower efficiencies for photovoltaics than those reported for 3D devices, despite their enhanced stability.[11] Recently, many bulky ammonium spacers, including allylammonium,[12] 2-thiophenemethylammonium,[13] phenylethylamine,[14] cyclohexylammonium,[15] and polyethylenimine,[16] have been studied to progressively improve the PCE of 2DRP PSCs. Ren and co-workers reported that the 2-(methylthio)ethylamine ($MTEA^+$) spacer can operate as an efficient bulky organic cation in 2DRP perovskites. The $MTEA^+$ spacer enables sulfur–sulfur (S–S) interactions, besides van der Waals forces, providing the perovskite lattice with improved charge-carrier dynamics and stabilization.[10] Later, Yin and co-workers introduced the $MTEA^+$ spacer into a tin-based 2DRP perovskite, which benefited from S–S non-covalent interactions. The authors demonstrated that these interactions induced the oriented crystallization of 2DRP perovskite, improved the film morphology, and reinforced the perovskite framework.[17]

However, most studies have focused on experimental evaluations of certain spacer cations, offering minimal theoretical understanding of the impact of device parameters and defect dynamics on photovoltaic performance. We wished to identify performance limits and dominant loss mechanisms for 2DRP PSCs. The reported high efficiency, therefore, represents an upper-bound scenario. We explored the optoelectronic characteristics of the lead-based 2DRP $(MTEA)_2(MA)_4Pb_5I_{16}$ (n = 5) perovskite with $MTEA^+$ interlayer spacers. Using 1D solar cell capacitance simulator (SCAPS-1D) calculations, we characterized the effects of perovskite layer thickness, trap-state density (N_{Trap}), and shallow acceptor density (N_A). After optimization, the 2DRP device achieved a maximum PCE of 18% with a high V_{OC} of 1.48 V. Then, we combined mobility-thickness-defect-density co-optimization to optimize 2DRP perovskite beyond 20% efficiency. Additionally, the $MTEA^+$-based 2DRP PSCs retained 95% of their initial performance under 420 K in the SCAPS-1D simulation, indicating a theoretically enhanced thermal tolerance.

2. Methodology

A SCAPS-1D model was developed by Burgelman and co-workers to simulate solar cells up to seven layers.[18] SCAPS-1D solves Poisson's and continuity equations for charge carriers to determine potential fields and charge-carrier kinetics, respectively. Additionally, current densities for an electron and a hole can be calculated by the drift-diffusion equation, as described in a previous report.[19] The trapping and de-trapping processes within traps in the energy gap can be explained by the Shockley–Read–Hall (SRH) recombination equation.[20] This software simulates the AC and DC electrical properties of heterojunction photovoltaics. It also assists in the calculation of several device performance parameters and charge-carrier dynamics. These include generation and recombination rates, incident-photon-to-current efficiency (IPCE), absorption coefficient (α), complex impedance (Z), built-in potential (V_{bi}), V_{OC}, J_{SC}, FF, and PCE.

The standard AM1.5G spectral illumination with an intensity of 1000 W m^{-2} at 300 K was utilized as input solar radiation for the calculation. We used fluorine-doped tin oxide (FTO) as an illuminated side with a flat-band contact and a gold (Au) electrode on an opaque side with a work function of 5.1 eV. SCAPS-1D simulations closely aligned with experimental findings when critical conditions such as parasitic resistances and interfacial and bulk defects were considered. We set the series resistance (R_S) and shunt resistance (R_{SH}) at 4 Ohm cm^2 and 1000 Ohm cm^2, respectively. Two interfacial layers with a trap-state density (N_{Trap}) of 10^{10} cm^{-2} were incorporated at the electron transport material (ETM)/perovskite and perovskite/hole transport material (HTM) interfaces (Table S1). The fundamental ETM, HTM, and absorber characteristics are listed in Table 1 and are derived from some earlier studies. The energetic distribution was considered as a single discrete level, rather than a Gaussian or exponential distribution, to simplify the recombination modeling while capturing the dominant trap-assisted recombination pathway.

Table 1 Key simulation parameters of the layers used in the device structure

Parameters (units)	FTO	TiO_2	$(MTEA)_2(MA)_4Pb_5I_{16}$	Spiro-OMeTAD
Thickness (nm)	300	50	350	100
Bandgap E_g (eV)	3.5	3.2	1.8	3.01
Electron affinity (eV)	4.0	4.05	3.6	2.18
Dielectric permittivity	9	33	12	3
Effective density of states in conduction band (cm^{-3})	2.2×10^{18}	1.0×10^{18}	1.0×10^{19}	2.2×10^{18}
Effective density of states in valence band (cm^{-3})	1.8×10^{19}	1.0×10^{19}	1.0×10^{18}	2.0×10^{17}
Electron mobility (cm^2 V^{-1} s^{-1})	20	18.5	1.3×10^{-2}	7.9×10^{-3}
Hole mobility (cm^2 V^{-1} s^{-1})	10	1.0×10^{-4}	1.7×10^{-2}	7.9×10^{-3}
Electron thermal velocity (cm s^{-1})	1.0×10^7	1.0×10^7	1.0×10^7	1.0×10^7
Hole thermal velocity (cm s^{-1})	1.0×10^7	1.0×10^7	1.0×10^7	1.0×10^7
Shallow donor density (cm^{-3})	2.0×10^{19}	1.0×10^{19}	—	—
Shallow acceptor density (cm^{-3})	—	—	1.0×10^{15}	1.2×10^{17}
Defect type	Neutral	Neutral	Neutral	Neutral
Trap-state density (cm^{-3})	1.0×10^{15}	1.0×10^{16}	2.22×10^{15}	1.0×10^{15}
Electron capture cross-section (cm^2)	1.0×10^{-16}	1.0×10^{-16}	1.0×10^{-16}	1.0×10^{-16}
Hole capture cross-section (cm^2)	1.0×10^{-16}	1.0×10^{-16}	1.0×10^{-16}	1.0×10^{-16}
Defect position above the valence band edge (eV)	0.6	0.6	0.6	0.6
Energetic distribution	Single	Single	Single	Single
References	21	22–24	10 and 25	26–28

3. Results and discussion

Fig. 1a shows the planned architecture of PSC. It contains typical 2,2′,7,7′-Tetrakis[*N*,*N*-di(4-methoxyphenyl)amino]-9,9′-spirobifluorene (spiro-OMeTAD) as the HTM, TiO_2 as the ETM, and 2DRP $(MTEA)_2(MA)_4Pb_5I_{16}$ (n = 5) perovskite as the absorber layer. Using $MTEA^+$ as the bulky ammonium can reinforce interlayer molecular interaction *via* S–S non-covalent interactions. The presence of organic spacers can improve the intrinsic properties of 2DRP in three main ways. First, by providing a lower dielectric constant layer, which increases quantum confinement and dielectric confinement and, thus, initiates a large exciton binding energy.[29] Second, it couples electrostatically with the inorganic framework, inducing structural distortion. Third, it regulates crystal growth, thereby affecting film morphology and quality.[30] Recently, heteroatomic molecular interaction in spacer cations has been shown to significantly modulate nucleation, perovskite layer growth, and phase stability through a combination of electrostatic, steric, and non-covalent interactions.[31] The energy band structure of the simulated PSC is exhibited in Fig. 1b. It reveals well-aligned conduction and valence bands that promote effective charge-carrier transfer and a limited recombination process. The appropriate band alignment allowed for a strong electric field at the 2DRP/spiro-OMeTAD contact, giving rise to hole extraction (Fig. 1c). Fig. 1d shows the *J*–*V* plot of the initial device from which the main photovoltaic parameters (*i.e.*, J_{SC}, FF, V_{OC}, and PCE) were extracted. The 2DRP cell obtained a PCE of 10.76% with a V_{OC} of 1.38 V, a J_{SC} of 14.39 mA cm^{-2}, and a FF of 53.93%. Improved band alignment gave rise to high quasi-Fermi level splitting (QFLS), thereby mitigating interfacial recombination and leading to a higher V_{OC}. The corresponding IPCE spectrum in Fig. 1e implied a wide photoresponse in the visible region. Fig. 1f displays the variations in α for the ETM, HTM, and absorber films using the default SCAPS optical absorption model. These findings indicated that the 2DRP perovskite dominated the visible spectrum with a band-edge region $>10^5$ cm^{-1} while the charge transport materials remained largely transparent with minimal contribution to light harvesting.

The perovskite film could have various defects, such as interstitials, vacancies, and grain boundaries, which would decrease the stability and efficiency of PSCs by acting as charge recombination sites. The N_{Trap} within the 2DRP perovskite was changed from 10^{14} to 10^{18} cm^{-3}, and the corresponding *J*–*V* plots are illustrated in Fig. 2a. All photovoltaic parameters were reduced progressively with increasing defects. As shown in Fig. 2b, a pronounced decline in J_{SC} could be assigned to increased non-radiative recombination sites, which lower charge-carrier extraction. Additionally, a higher N_{Trap} reduces carrier lifetime, shrinks the QFLS, and thereby limits V_{OC}.[32] Consequently, the PCE of devices decreased from 15.35% to 0.22% with defects varying from 10^{14} to 10^{18} cm^{-3} (Fig. 2c). The reduction of IPCE spectra across the visible range in Fig. 2d further confirmed the suppression in charge collection and J_{SC}. Fig. 2e shows Nyquist plots derived from *C*–*f* measurements for PSCs at different N_{Trap} values. The results demonstrated a narrowing in semicircles at elevated traps, implying a decrease in recombination resistance (R_{rec}). These findings were corroborated

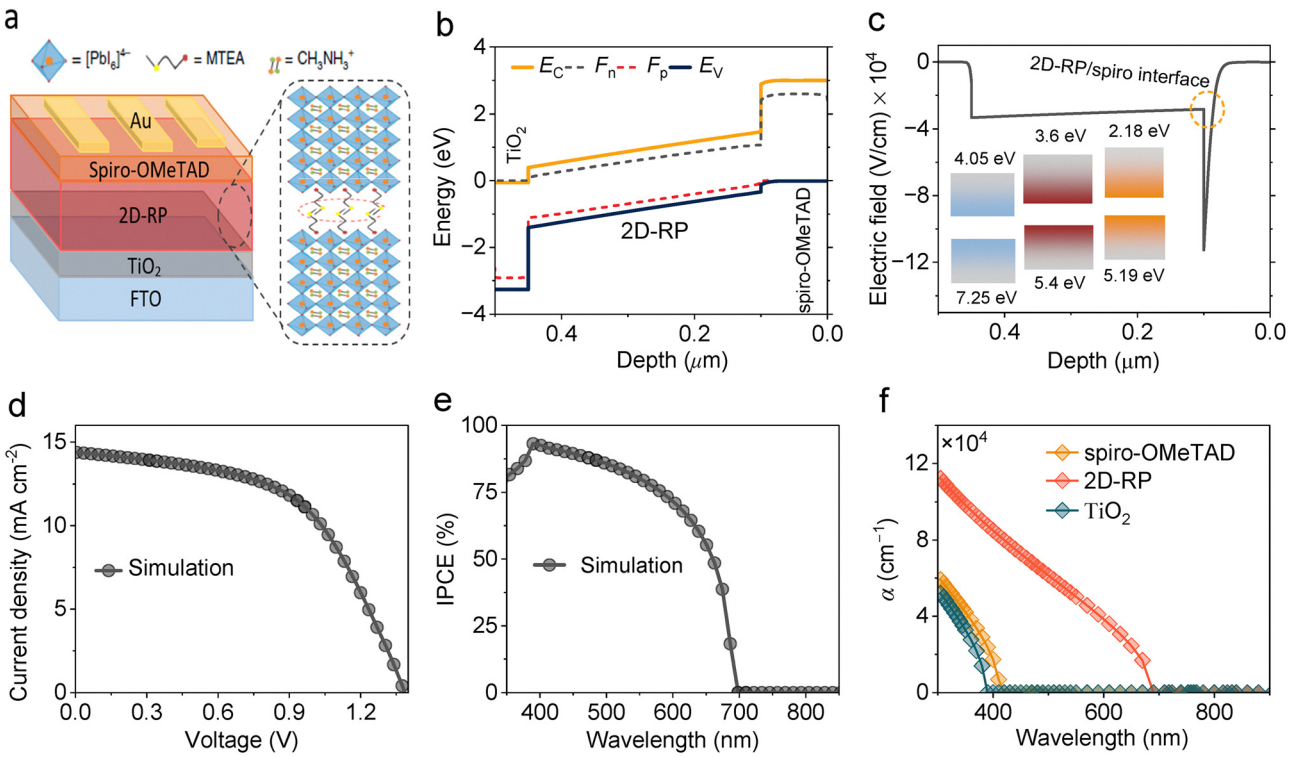

Fig. 1 Schematic illustration and initial calculations of the proposed PSC structure. (a) Layered structure of the device. (b) Band diagram of the PSC. (c) Electric field distribution. Inset: energy level alignment. (d) *J*–*V* plot of the simulated device under AM1.5 illumination. (e) IPCE spectrum. (f) Absorption coefficient as a function of wavelength.

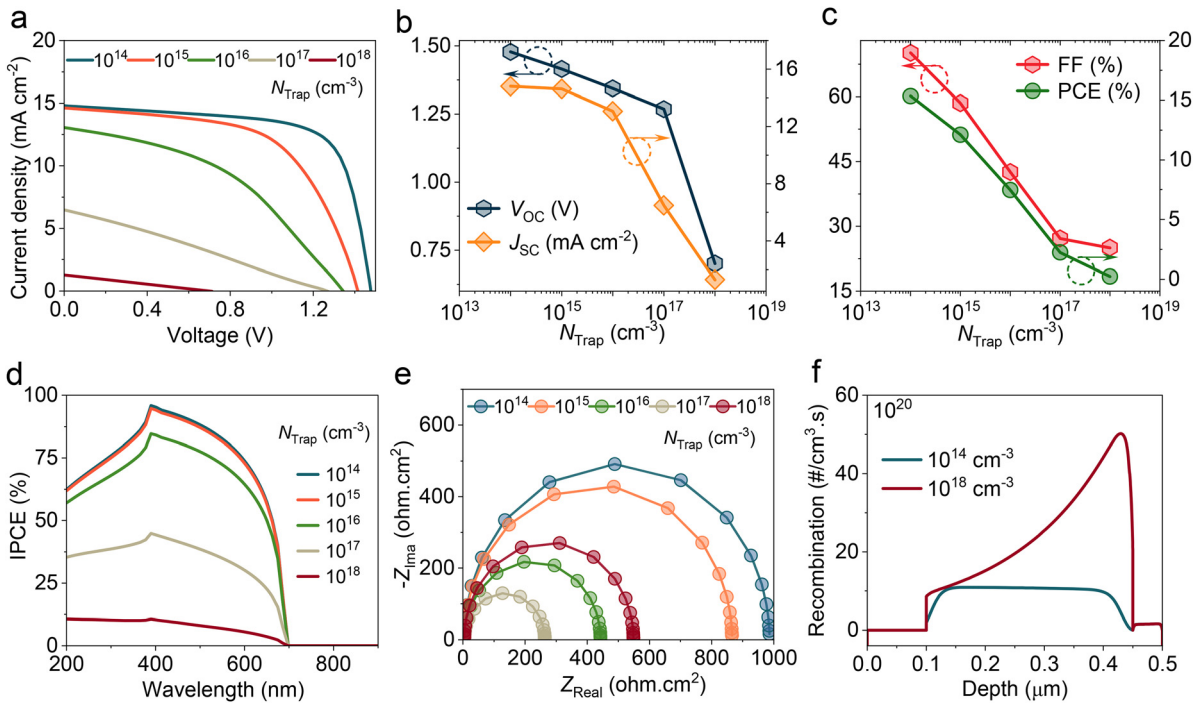

Fig. 2 Effect of defect density within a perovskite on the performance of 2DRP-based PSCs. (a) *J–V* characteristics. (b) Dependency of V_{OC} and J_{SC} on N_{Trap}. (c) Evaluation of FF and PCE with N_{Trap}. (d) IPCE curves. (e) Nyquist plots derived from impedance measurements under AC perturbation. (f) Recombination rate at low and high N_{Trap} concentrations.

by recombination curves in Fig. 2f, which showed that a higher N_{Trap} accelerated the recombination rate throughout the 2DRP absorber. According to the SRH equation,[20] if N_{Trap} is passivated, charge carrier lifetime increases and, hence, longer diffusion length and less recombination are reported. The best-performing device achieved a PCE of 15.35% at an N_{Trap} of 10^{14} cm^{-3} and a charge-carrier diffusion length of 580 nm, which lies within the experimentally reported value.[33,34] Moreover, research shows that 2D and quasi-2D perovskites usually have a lower N_{Trap} than 3D perovskite frameworks. This is because of organic spacer cations and passivation effects, which support the idea of low trap density states.[35]

Increasing the perovskite thickness generally results in more photons being harvested, but thicker perovskites can be detrimental to carrier generation if carrier diffusion lengths are small. To evaluate how the PSC parameters are affected by the absorber thickness, the perovskite layer thickness was varied within a range of 200 nm to 600 nm. The obtained *J–V* characteristics are displayed in Fig. 3a. The device V_{OC} was nearly constant, and J_{SC} improved significantly from 11.52 to 16.54 mA cm^{-2} while increasing the 2DRP thickness from 200 to 600 nm (Fig. 3b). This current enhancement was due to an increasing photoresponse across the visible spectrum, enabling a high number of photo-induced carriers, as confirmed by IPCE curves in Fig. 3d. However, FF decreased moderately with an increase in thickness due to increasing trap-assisted recombination and the saturation current (Fig. 3c). A higher charge carrier recombination at a thick perovskite was further supported by decreasing R_{rec} (Fig. 3e) and increasing recombination rate (Fig. 3f). The simulated recombination R_{rec} had only a slight reduction (inset of Fig. 3e) because, under the fixed interface defect concentration and transport-layer properties utilized in our simulation, recombination was primarily limited by interface processes rather than bulk thickness effects. We selected the optimal thickness of 2DRP as 500 nm for further calculations. The PSC parameters were V_{OC} = 1.47 V, J_{SC} = 16.43 mA cm^{-2}, FF = 67.55%, and PCE = 16.38%.

R_{SH} and R_S, which have a significant effect on solar cell performance, determine the shape and slope of *J–V* properties. In fact, R_S originates from the electrical resistance of electrodes, as well as from the electrical dissipation that takes place in the perovskite, HTM, and ETM. Several carrier recombination pathways emerge as R_{SH}, which is also greatly impacted by device architecture. Therefore, a low R_{SH} could impact the collected photocurrent and cause a loss in photovoltage.[36]

Fig. 4a shows the *J–V* plots of 2DRP-based PSCs at different R_S while maintaining R_{SH} at 1000 Ohm cm^2. For an R_S > 8 Ohm cm^2, J_{SC} was downshifted slightly to 16.31 mA cm^{-2} (Fig. 4b). An increment in R_S decreased the FF from 68.95% to 60.65% of PSCs. Consequently, the overall performance fell rapidly from 16.75% to only 14.55% due to ohmic losses that limited carrier extraction (Fig. 4c). Fig. 4d shows the *J–V* plots for various R_{SH} ranging from 1000 to 5000 Ohm cm^2. The J_{SC} and V_{OC} remained constant as R_{SH} increased (Fig. 4e), but FF and efficiency gradually improved as R_{SH} increased (Fig. 4f). A higher R_{SH} reduces leakage pathways and minimizes parasitic recombination, leading to improved charge collection efficiency, as evidenced by the Nyquist plots in Fig. S1. At 5000 Ohm cm^2, we

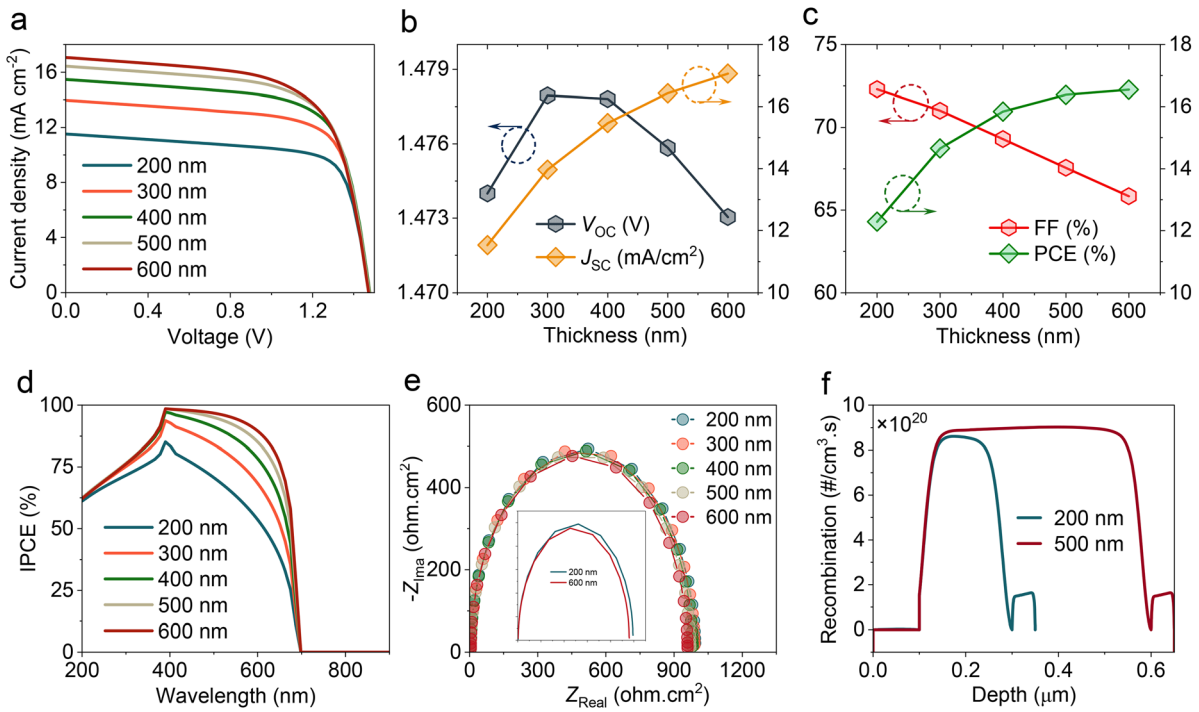

Fig. 3 Effect of perovskite layer thickness on the performance of 2DRP-based PSCs. (a) J–V characteristics. (b) Variation of V_{OC} and J_{SC}. (c) Evaluation of FF and PCE. (d) IPCE spectra. (e) Nyquist plots. (f) Recombination rate profiles at thicknesses of 200 nm and 500 nm.

obtained an FF = 73.52% and PSC = 18%. These trends in PSC behavior align well with the literature.[37]

To probe the behaviour of PSCs in an operating environment, we evaluated the performance of the PSC by changing the temperature from 300 K to 420 K. Fig. 4g depicts the J–V curves of simulated devices. Fig. 4h exhibits the tracking of normalized PCEs with temperature. V_{OC} and PCE were slightly reduced with an increase in temperature, indicating a predication for high thermal stability. This reduction in PCE occurred because, as temperature rises, the reverse saturation current increases. Moreover, the increasing temperature can result in the thermal excitation of electrons, causing some vibrations and eventual instability, and improving charge-carrier recombination rates. Optimized devices maintained 95% of their initial efficiency at 420 K compared with 88% thermal stability for non-optimized devices (control), predicting high thermal stability. In SCAPS-1D, temperature influences carrier transport, recombination, and energy band alignment, but does not account for thermally induced degradation mechanisms such as phase decomposition, ion migration, or material volatilization. Therefore, the anticipated high thermal stability represented an upper performance limit under steady-state conditions rather than long-term operational durability.

For further optimization of 2DRP PSCs, we increased charge-carrier mobility from 10^{-5} to 0.1 cm^2 V^{-1} s^{-1}, which could be achieved experimentally by the vertical orientation of 2DRP films with heteroatom-containing spacers or employing spacers with stronger interlayer interactions. The improved mobility suppressed space-charge accumulation, thus lowering recombination rates and improving charge collection. Therefore, the simulated PSC realized a PCE of 20.79%, with a J_{SC} of 17.17 mA cm^{-2}, a V_{OC} of 1.49 V, and an FF of 81.03% (Fig. S2). The substantial increase in V_{OC} and FF indicates that improved vertical transport mitigated non-radiative losses. The inherent semiconducting characteristics of the 2DRP perovskite and relatively wide bandgap (1.8 eV), which sets a high theoretical V_{OC} limit, allowed high V_{OC} values in the optimized PSCs. Additionally, optimizing the defect density, band alignment, and charge mobility enabled QFLS to approach this thermodynamic limit with only a V_{OC} deficit of 0.32 eV. Experimental results of charge transport in 2DRP perovskites have shown an effective carrier mobility in the range of 8.0 ± 0.6 cm^2 V^{-1} s^{-1} for layered frameworks such as PEA_2PbI_4.[38] Therefore, the carrier mobilities utilized in our theoretical calculations were consistent with optimized transport conditions and oriented films.

To analyze the influence of the transparent conducting oxide (TCO) and short-wavelength photons, a 300 nm-thick FTO film was included in the SCAPS-1D simulation. As shown in Fig. S3, inclusion of FTO led to an efficiency of 20.28% compared with 20.79% attained using the default TCO arrangement, with the minor decrease originating from reductions in J_{SC} and FF, while V_{OC} remained constant. We can state that the simulated 2DRP PSC was reliable even with applying TCO and that UV photons did not have a significant role in determining the overall performance.

To evaluate the effectiveness of our simulated PSC, we compared the PCE of our designed PSC with previously reported devices. Fig. 5 displays a comparative diagram for the state-of-the-art rigid PSCs reported in the literature. As exhibited in Fig. 5, the simulated PSC shows a competitive performance, positioning

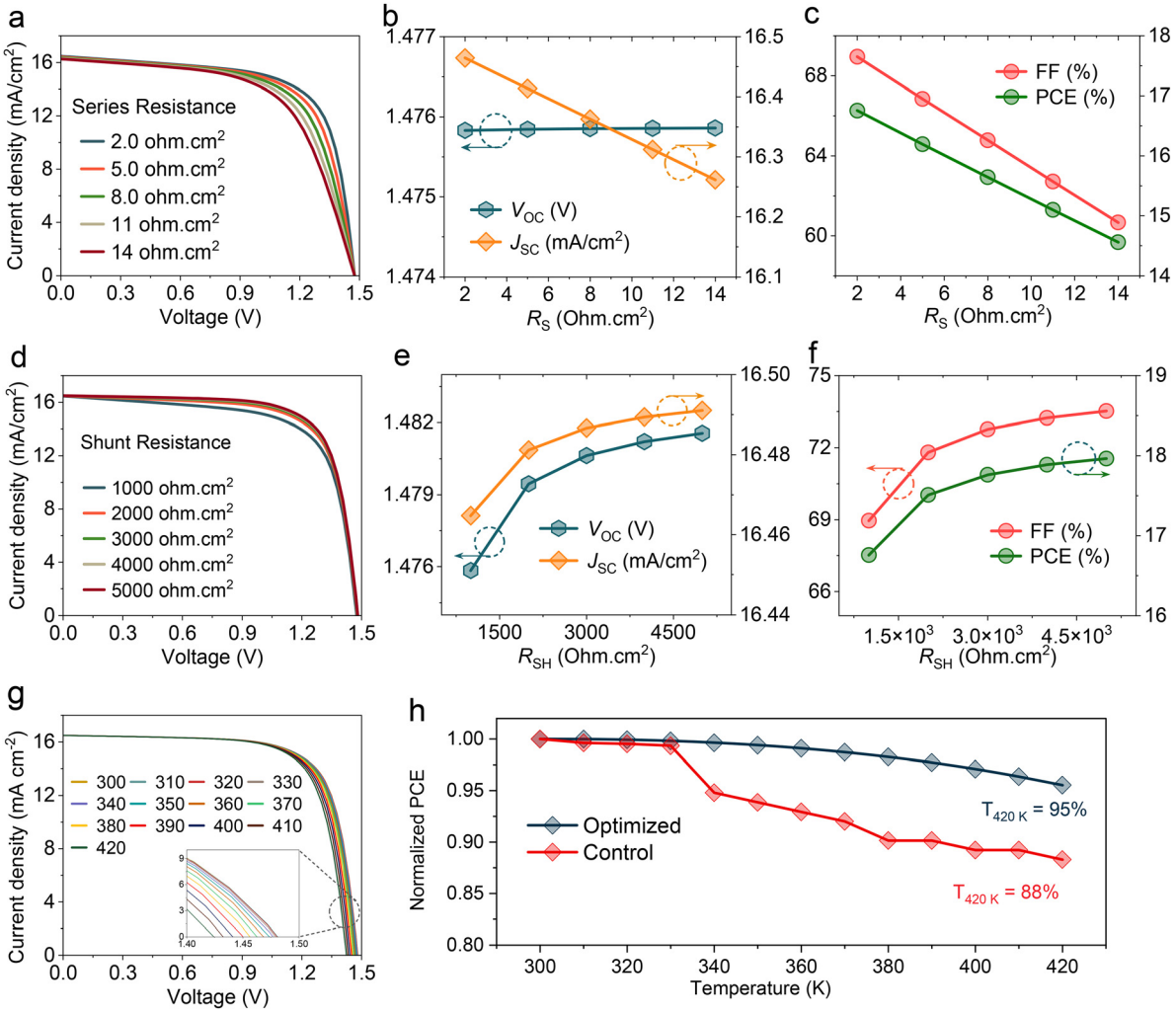

Fig. 4 Influence of resistive losses and operating temperature upon device performance. (a) J–V characteristics with varying R_S. (b) Variation of V_{OC} and J_{SC}. (c) Evaluation of FF and PCE. (d) J–V plots with changing R_{SH}. (e) Variation of V_{OC} and J_{SC}. (f) FF and PCE changing with R_{SH}. (g) J–V curves at different temperatures. (h) Normalized PCEs.

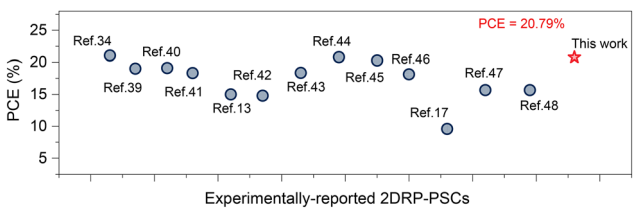

Fig. 5 Summary of the performances for the state-of-the-art rigid PSCs with 2DRP absorber reported in the literature.[13,17,34,39–48]

among the top-performing PSCs. This emphasizes how successfully $MTEA^+$ cation spacer incorporation and material optimization improve device stability and efficiency.

4 Conclusions

We designed a solar cell based on 2DRP hybrid perovskite incorporating $MTEA^+$ bulky spacers with S–S non-covalent interactions, contributing to structural stability and enhanced photoelectric performance. Then, we systematically simulated 2DRP-based PSCs using SCAPS-1D software. Trap density within the perovskite critically influenced solar cell performance by accelerating trap-assisted recombination, reducing carrier lifetime and diffusion length, and thereby degrading all device parameters. The best performance was obtained with a standard thin perovskite absorber of thickness of 500 nm, balancing between effective photon absorption and carrier transport. Moreover, an increase in R_S led to reduced charge extraction, degraded FF, and lowered efficiency. An increase in R_{SH} enhanced charge-carrier selectivity and suppressed leakage losses, resulting in higher FF and efficiency. Consequently, the PSCs proposed with $(MTEA)_2(MA)_4Pb_5I_{16}$ (n = 5) achieved an efficiency of 20.79% with a high V_{OC} of 1.49 V. Importantly, the strengthened interlayer molecular interactions were found theoretically to support thermal robustness above 420 K, positioning 2DRP perovskites as a highly promising class of materials. Generally, we report theoretical performance limits in 2DRP PSCs, with the reported high PCEs representing upper-bound

scenarios achievable only under optimized charge-transport conditions.

Conflicts of interest

The authors declare no conflict of interest.

Data availability

Data will be available from the corresponding author upon reasonable request.

Supplementary information (SI) is available. See DOI: https://doi.org/10.1039/d5ya00364d.

References

1 H. Togun, A. Basem, A. A. H. Kadhum, A. M. Abed, N. Biswas, F. L. Rashid, R. A. Lawag, H. M. Ali, H. I. Mohammed and D. K. Mandal, Advancing photovoltaic thermal (PV/T) systems: Innovative cooling technique, thermal management, and future prospects, *Sol. Energy*, 2025, **291**, 113402.
2 A. Basem, S. Opakhai, Z. M. S. Elbarbary, F. Atamurotov and N. E. Benti, A comprehensive analysis of advanced solar panel productivity and efficiency through numerical models and emotional neural networks, *Sci. Rep.*, 2025, **15**(1), 259.
3 H. Togun, A. Basem, M. J. Jweeg, N. Biswas, A. M. Abed, D. Paul, H. I. Mohammed, A. Chattopadhyay, B. K. Sharma and T. Abdulrazzaq, Advancing organic photovoltaic cells for a sustainable future: The role of artificial intelligence (AI) and deep learning (DL) in enhancing performance and innovation, *Sol. Energy*, 2025, **291**, 113378.
4 H. Dong, C. Ran, W. Gao, M. Li, Y. Xia and W. Huang, Metal Halide Perovskite for next-generation optoelectronics: progresses and prospects, *ELight*, 2023, **3**(1), 3.
5 F. A. Nelson, A. Basem, D. J. Jasim, T. E. Gber, M. T. Odey, A. F. Al Asmari and S. Islam, Chemical effect of alkaline-earth metals (Be, Mg, Ca) substitution of BFe2XH hydride perovskites for applications as hydrogen storage materials: A DFT perspective, *Int. J. Hydrogen Energy*, 2024, **79**, 1191–1200.
6 Best Research-Cell Efficiency Chart, 2025. https://www.nrel.gov/pv/cell-efficiency.html.
7 W. Feng, R. Zhao, X. Wang, B. Xing, Y. Zhang, X. He and L. Zhang, Global instability index as a crystallographic stability descriptor of halide and chalcogenide perovskites, *J. Energy Chem.*, 2022, **70**, 1–8.
8 Z. Zhang, J. Jin, Z. Li, Y. Huang, Y. Jiang, M. Li, C. Wang, Y. Luo, Z. Gao and Y. Xu, Nucleation-Layer Assisted Quasi-2D Ruddlesden-Popper Tin Perovskite Solar Cells with High Oxygen Stability, *Adv. Mater.*, 2025, 2501156.
9 X. Dong, X. Li, X. Wang, Y. Zhao, W. Song, F. Wang, S. Xu, Z. Miao and Z. Wu, Improve the charge carrier transporting in two-dimensional Ruddlesden–Popper perovskite solar cells, *Adv. Mater.*, 2024, **36**(19), 2313056.
10 H. Ren, S. Yu, L. Chao, Y. Xia, Y. Sun, S. Zuo, F. Li, T. Niu, Y. Yang and H. Ju, Efficient and stable Ruddlesden–Popper perovskite solar cell with tailored interlayer molecular interaction, *Nat. Photonics*, 2020, **14**(3), 154–163.
11 U. Gunes, F. V. Yaylali, Z. G. Karabag, X.-X. Gao, O. A. Syzgantseva, A. Karabag, G. B. Yildirim, K. Tsoi, N. Shibayama and H. Kanda, Drastic influence of substituent position on orientation of 2D layers enables efficient and stable 3D/2D perovskite solar cells, *Cell Rep. Phys. Sci.*, 2023, **4**(5), 101380.
12 A. H. Proppe, R. Quintero-Bermudez, H. Tan, O. Voznyy, S. O. Kelley and E. H. Sargent, Synthetic control over quantum well width distribution and carrier migration in low-dimensional perovskite photovoltaics, *J. Am. Chem. Soc.*, 2018, **140**(8), 2890–2896.
13 H. Lai, B. Kan, T. Liu, N. Zheng, Z. Xie, T. Zhou, X. Wan, X. Zhang, Y. Liu and Y. Chen, Two-dimensional Ruddlesden–Popper perovskite with nanorod-like morphology for solar cells with efficiency exceeding 15%, *J. Am. Chem. Soc.*, 2018, **140**(37), 11639–11646.
14 L. N. Quan, M. Yuan, R. Comin, O. Voznyy, E. M. Beauregard, S. Hoogland, A. Buin, A. R. Kirmani, K. Zhao and A. Amassian, Ligand-stabilized reduced-dimensionality perovskites, *J. Am. Chem. Soc.*, 2016, **138**(8), 2649–2655.
15 S. Jeong, S. Seo, H. Yang, H. Park, S. Shin, H. Ahn, D. Lee, J. H. Park, N. G. Park and H. Shin, Cyclohexylammonium-based 2D/3D perovskite heterojunction with funnel-like energy band alignment for efficient solar cells (23.91%), *Adv. Energy Mater.*, 2021, **11**(42), 2102236.
16 K. Yao, X. Wang, Y.-X. Xu, F. Li and L. Zhou, Multilayered perovskite materials based on polymeric-ammonium cations for stable large-area solar cell, *Chem. Mater.*, 2016, **28**(9), 3131–3138.
17 M. Yin, H. Yao, C. Wu, P. Yan, L. Ding and F. Hao, Highly oriented and efficient 2D ruddlesden-popper tin halide perovskite solar cells with enhanced intermolecular interactions, *Chem. Eng. J.*, 2025, **511**, 162111.
18 M. Burgelman, P. Nollet and S. Degrave, Modelling polycrystalline semiconductor solar cells, *Thin Solid Films*, 2000, **361**, 527–532.
19 H. R. Abdul Ameer, A. N. Jarad, K. H. Salem, H. S. Hadi, M. A. Alkhafaji, R. S. Zabibah, K. A. Mohammed, K. Kumar Saxena, D. Buddhi and H. Singh, A role of back contact and temperature on the parameters of CdTe solar cell, *Adv. Mater. Process. Technol.*, 2024, **10**(2), 497–505.
20 T. I. Alanazi, A. Shaker and W. Zein, Design and simulation of 2D Ruddlesden–Popper perovskite solar cells under LED illumination: role of ETL and front contact band alignment, *Sol. Energy Mater. Sol. Cells*, 2024, **274**, 112992.
21 S. Mattaparthi, D. K. Sinha, A. Bhura and R. Khosla, Design of an eco-friendly perovskite Au/NiO/FASnI$_3$/ZnO0. 25S0. 75/FTO, device structure for solar cell applications using SCAPS-1D, *Results Opt.*, 2023, **12**, 100444.
22 J.-i Fujisawa, T. Eda and M. Hanaya, Comparative study of conduction-band and valence-band edges of TiO_2, $SrTiO_3$, and $BaTiO_3$ by ionization potential measurements, *Chem. Phys. Lett.*, 2017, **685**, 23–26.
23 S. Mondal and A. Kumar, Tunable dielectric properties of TiO2 thin film based MOS systems for application in microelectronics, *Superlattices Microstruct.*, 2016, **100**, 876–885.

24 T. S. Krasienapibal, T. Fukumura, Y. Hirose and T. Hasegawa, Improved room temperature electron mobility in self-buffered anatase TiO2 epitaxial thin film grown at low temperature, *Jpn. J. Appl. Phys.*, 2014, **53**(9), 090305.
25 X. Zhong, X. Ni, S. Sidhik, H. Li, A. D. Mohite, J. L. Brédas and A. Kahn, Direct Characterization of Type-I Band Alignment in 2D Ruddlesden–Popper Perovskites, *Adv. Energy Mater.*, 2022, **12**(45), 2202333.
26 S. Park, J. H. Heo, C. H. Cheon, H. Kim, S. H. Im and H. J. Son, A [2, 2] paracyclophane triarylamine-based hole-transporting material for high performance perovskite solar cells, *J. Mater. Chem. A*, 2015, **3**(48), 24215–24220.
27 N. J. Jeon, H. G. Lee, Y. C. Kim, J. Seo, J. H. Noh, J. Lee and S. I. Seok, o-Methoxy substituents in spiro-OMeTAD for efficient inorganic–organic hybrid perovskite solar cells, *J. Am. Chem. Soc.*, 2014, **136**(22), 7837–7840.
28 H. Ashassi-Sorkhabi and P. Salehi-Abar, How the change of OMe substituent position affects the performance of spiro-OMeTAD in neutral and oxidized forms: theoretical approaches, *RSC Adv.*, 2018, **8**(33), 18234–18242.
29 J. Zhang, J. Qin, M. Wang, Y. Bai, H. Zou, J. K. Keum, R. Tao, H. Xu, H. Yu and S. Haacke, Uniform permutation of quasi-2D perovskites by vacuum poling for efficient, high-fill-factor solar cells, *Joule*, 2019, **3**(12), 3061–3071.
30 R. Yang, R. Li, Y. Cao, Y. Wei, Y. Miao, W. L. Tan, X. Jiao, H. Chen, L. Zhang and Q. Chen, Oriented quasi-2D perovskites for high performance optoelectronic devices, *Adv. Mater.*, 2018, **30**(51), 1804771.
31 W. Gao, R. Huang, H. Dong, W. Li, Z. Wu, Y. Chen and C. Ran, Heteroatomic molecules for coordination engineering towards advanced Pb-free Sn-based perovskite photovoltaics, *Chem. Soc. Rev.*, 2025, 1384–1428.
32 E. Gutierrez-Partida, M. Rusu, F. Zu, M. Raoufi, J. Diekmann, N. Tokmoldin, J. Warby, D. Menzel, F. Lang and S. Shah, Toward understanding the built-in field in perovskite solar cells through layer-by-layer surface photovoltage measurements, *ACS Appl. Mater. Interfaces*, 2025, **17**(7), 11176–11186.
33 S. Shrestha, X. Li, H. Tsai, C.-H. Hou, H.-H. Huang, D. Ghosh, J.-J. Shyue, L. Wang, S. Tretiak and X. Ma, Long carrier diffusion length in two-dimensional lead halide perovskite single crystals, *Chem*, 2022, **8**(4), 1107–1120.
34 M. Shao, T. Bie, L. Yang, Y. Gao, X. Jin, F. He, N. Zheng, Y. Yu and X. Zhang, Over 21% efficiency stable 2D perovskite solar cells, *Adv. Mater.*, 2022, **34**(1), 2107211.
35 X. Gao, X. Zhang, W. Yin, H. Wang, Y. Hu, Q. Zhang, Z. Shi, V. L. Colvin, W. W. Yu and Y. Zhang, Ruddlesden–popper perovskites: synthesis and optical properties for optoelectronic applications, *Adv. Sci.*, 2019, **6**(22), 1900941.
36 Y. Li, B. Ding, Q.-Q. Chu, G.-J. Yang, M. Wang, C.-X. Li and C.-J. Li, Ultra-high open-circuit voltage of perovskite solar cells induced by nucleation thermodynamics on rough substrates, *Sci. Rep.*, 2017, **7**(1), 46141.
37 S. Karthick, S. Velumani and J. Bouclé, Experimental and SCAPS simulated formamidinium perovskite solar cells: A comparison of device performance, *Sol. Energy*, 2020, **205**, 349–357.
38 M. Kober-Czerny, S. G. Motti, P. Holzhey, B. Wenger, J. Lim, L. M. Herz and H. J. Snaith, Excellent Long-Range Charge-Carrier Mobility in 2D Perovskites, *Adv. Funct. Mater.*, 2022, **32**(36), 2203064.
39 Q. Fu, M. Chen, Q. Li, H. Liu, R. Wang and Y. Liu, Selenophene-based 2D Ruddlesden-Popper perovskite solar cells with an efficiency exceeding 19%, *J. Am. Chem. Soc.*, 2023, **145**(39), 21687–21695.
40 Y. Tang, X. Dong, X. Li, Y. Zhou, C. Ran and Z. Wu, Two-dimensional Ruddlesden-Popper perovskite solar cells with an efficiency exceeding 19% by inserting a self-assembled monolayer, *Chem. Eng. J.*, 2024, **499**, 156503.
41 K. Li, S. Yue, X. Li, N. Ahmad, Q. Cheng, B. Wang, X. Zhang, S. Li, Y. Li and G. Huang, High efficiency perovskite solar cells employing Quasi-2D Ruddlesden-Popper/Dion-Jacobson heterojunctions, *Adv. Funct. Mater.*, 2022, **32**(21), 2200024.
42 Z. Liu, L. Wang, H. Zhao, Y. Wei, X. Xie and P. Chen, High-performance Ruddlesden–Popper two-dimensional perovskite solar cells using integrated electron transport materials of tin oxide and indacenodithiophene, *Mater. Adv.*, 2023, **4**(16), 3551–3558.
43 X. Dong, Y. Tang, Y. Li, X. Li, Y. Zhao, W. Song, F. Wang, S. Xu, Y. Zhou, C. Ran, Z. Miao, L. Song and Z. Wu, Boosting MA-based two-dimensional Ruddlesden-Popper perovskite solar cells by incorporating a binary spacer, *J. Energy Chem.*, 2024, **95**, 348–356.
44 X. Dong, H. Zhang, J. Li, L. Yang, Y. Ma, H. Liu, Z. Hu and Y. Liu, Semiconductor Spacer with Donor-Acceptor Structure Drives 2D Ruddlesden–Popper Perovskite Solar Cells Beyond 20% Efficiency, *Angew. Chem., Int. Ed.*, 2025, **64**(22), e202501210.
45 X. Li, X. Dong, Z. Shen, X. Zai, Y. Li, Z. Miao, L. Song and Z. Wu, Halogenated Chiral Organic Spacer Cation Regulation for Efficient and Stable 2D Ruddlesden-Popper Perovskite Solar Cells, *Adv. Funct. Mater.*, 2025, 2507591.
46 Y. Zhang, R. Wang, H. Lu, M. Chen, H. Wang, T. He, T. Shao, Y. Liu, Y. Chen and G. Long, Alkyl Fluorination Aromatic Acetamidine Cation Enhances the Lattice Stability and Performance of 2D Ruddlesden-Popper Perovskite Solar Cells, *Small*, 2025, **21**(11), 2410546.
47 A. Wang, S. Chen, K. Du, Z. Fang, L. Zhang, L. Li, X. Dong, N. Yuan and J. Ding, Enhancing Vertical Orientation via Self-Assembled Molecule Interlayer Enables Efficient Ruddlesden–Popper Perovskite Solar Cells, *Solar RRL*, 2025, **9**(7), 2400906.
48 C. Yuan, Z. Zhang, S. Tang, Y. Gou, P. Zhao, H. Li and H. Yu, Cooperation of Dual Organic Spacers and A Site Cations for High-Performance Quasi-2D Ruddlesden–Popper Perovskite Solar Cells, *ChemPlusChem*, 2025, 2500169.